Composite Structures 210 (2019) 310–320

Contents lists available at ScienceDirect

Composite Structures

journal homepage: www.elsevier.com/locate/compstruct

Selective activation of intrinsic cohesive elements for fracture analysis of laminated composites

Kyeongsik Woo[a,*], Douglas S. Cairns[b]

[a] Chungbuk National University, School of Civil Engineering, Cheongju, Chungbuk, Republic of Korea
[b] Montana State University, Department of Mechanical and Industrial Engineering, Bozeman, MT, USA

ARTICLE INFO

Keywords:
Selective activation of cohesive elements
Controllable MPC
Cohesive zone modeling
Laminated composites
Progressive failure analysis

ABSTRACT

In this paper, we studied the selective activation of intrinsic cohesive elements by using controllable multi-point constraints (MPCs) for fracture analyses of laminated composites. Cohesive elements inserted between bulk elements were deactivated by tying the cohesive nodes using MPC, which were selectively activated during analysis only for the failure region by releasing the constraints. A strategy for the systematic definition and release of MPCs that considers the composite failure modes was developed. When applied to the fracture analysis of laminated composites, the selective activation strategy was found to alleviate the artificial compliance problem of intrinsic cohesive elements while producing results that matched accurately those of conventional intrinsic cohesive elements.

1. Introduction

There has been continued interest in composite materials over the past several decades. Composite materials have excellent specific stiffness/strength properties compared to conventional materials. The application of composite materials has increased in advanced aerospace structures, and it is gradually expanding into structures in the general industrial sector. In laminated composites, failure occurs in a complex combination of diverse failure modes at the fiber, matrix and interface regions [1]. An accurate understanding of failure behavior is crucial for the design of efficient composite structures with structural integrity. A vast amount of experimental, analytical and numerical studies have been performed to investigate how failures, which include failure criteria and progressive failure models, initiate and propagate in composite materials. The failure behavior of laminated composites with stress concentrators, such as a hole and a notch, bears a particular importance. This problem has been extensively studied by a number of researchers (e.g., [2–5]). When a tensile load is applied to both ends of a notched composite laminate, stress concentration develops at the notch tip, and matrix cracking and interlayer delamination start and propagate. These damages continuously interact with each other and grow until fiber breakage finally occurs, leading to ultimate failure.

Numerical simulation is becoming a more efficient way to study the progressive fracture behavior of composite materials owing to the development of very fast computer hardware and reliable analysis software. Frequently used numerical methods include the virtual crack closure technique (VCCT) (e.g., [6,7]), continuum damage mechanics (CDM) (e.g., [8–14]), cohesive zone modeling (CZM) (e.g., [15–20]), and extended finite element method (XFEM) (e.g., [21,22]). VCCT is a linear elastic fracture mechanics (LEFM)-based method in which a crack is allowed to propagate when the calculated strain energy release rate (G) is larger than the material fracture energy (G_c). Although proven to be accurate in predicting crack propagation behavior, this method requires an initial crack and an a priori knowledge of the crack path. CDM, also known as progressive failure analysis, simulates failure behavior in such a way that the damage initiation is predicted by a failure criterion first, and then the corresponding material is softened by a property degradation model. This method has been developed quite well and is widely used; however, it is well-known to suffer from the mesh-dependence problem [23]. In CZM, material failure is explicitly described by interface elements inserted between bulk elements and by a constitutive relation called traction-separation law (TSL). CZM removes the initial crack requirement of the VCCT and provides much better mesh regularization characteristics compared to a CDM-based method. However, intrinsic CZM with the initially elastic TSL not only can alter the elastic bulk response but also can affect the fracture solution [24,25]. With extrinsic CZM, by inserting cohesive elements adaptively only as needed, it can avoid the effect of the added compliance problem; however, a sophisticated management of complex data structures is required because finite element meshes have to be

* Corresponding author.
E-mail address: kw3235@chungbuk.ac.kr (K. Woo).

https://doi.org/10.1016/j.compstruct.2018.11.055
Received 20 June 2018; Received in revised form 28 October 2018; Accepted 20 November 2018
Available online 22 November 2018

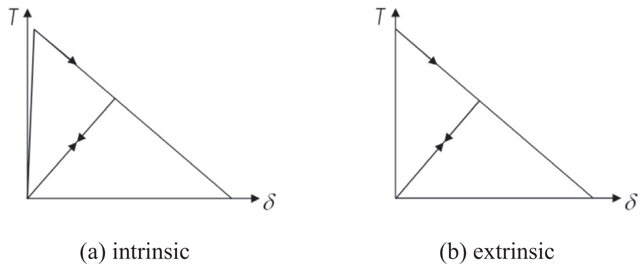

Fig. 1. Intrinsic and extrinsic traction-separation laws.

changed continuously during the analysis [25–27]. In XFEM, cracks are represented by a local enrichment through the partition of unity concept and level sets which offers significant advantages such as having superior convergence rates in problems with discontinuities and singularities. It is a very promising method that eliminates the mesh-dependence problem, and studies are being performed for further development to be applied to composite fracture problems with multi-failures.

With these methods, researchers are able to successfully predict the initiation and propagation of composite failure. There have been studies employing the above methods in combination such as mixed CDM/CZM (e.g., [28,29]), XFEM/CZM (e.g., [5,30]) or discontinuous Galerkin/CZM (DG/CZM) methods [31] to maximize the merits while avoiding the demerits of each method.

Recently, CZM has been increasingly used for fracture analysis of composite materials because of its advantages such as providing an explicit and clear picture of the physical representation of cracks and ease of implementation within the conventional finite element method. CZM is categorized into two groups depending on which TSL is used: intrinsic and extrinsic [32]. As shown in Fig. 1(a), intrinsic CZM uses TSLs that have an initially elastic region before the onset of fracture. In this case, a finite element model appears softer owing to the finite initial stiffness, which creates the well-known artificially added compliance problem. The added compliance effect may not be too much of a concern for problems with discrete line-(2D) or surface-like (3D) crack propagation, as in, for example, delamination or interface separation where a small number of cohesive elements are inserted. However, it becomes particularly significant for problems with distributed area-(2D) or volume-like (3D) damage, as in, for example, the simulations of distributed matrix damage where a large number of cohesive elements have to be inserted between every bulk element throughout the expected damage area or volume. This explains why CZM has been used mostly to model delamination, whereas CDM is used to model, for example, in fracture analysis of laminated composites.

The artificial compliance problem may be minimized using an alternative method known as extrinsic CZM [25–27]. In this case, cohesive elements whose cohesive behavior is defined by an initially rigid, but strictly decreasing, TSL, as shown in Fig. 1(b), are adaptively inserted into the mesh only as needed during the analysis. However, a sophisticated management of complex data structures is required because finite element meshes have to be changed continuously by the insertion of new cohesive elements as damage propagates. Because of this, extrinsic CZM is extremely difficult to implement and can have a low scalability for parallel computation of large-size problems [25,31].

For the alleviation of the added compliance problem of intrinsic CZM, a selective activation strategy under the intrinsic CZM framework was developed in Ref. [33]. The core of this strategy is to insert cohesive elements and deactivate them by tying the duplicated nodes using multi-point constraints (MPCs) before analysis and then to selectively activate part of the cohesive elements as needed during analysis by controlling the MPCs. There is no complexity involved in data structure management because of the insertion at the beginning, and the added compliance effect is reduced because only a small number of cohesive elements are activated. Conceptually this idea is similar to the CZM/DG method developed in Ref. [31], in which the continuity between bulk elements during the pre-fracture stage is ensured by the consistent DG interface terms. However, the MPC-controlled activation strategy is more attractive as it can be implemented easily using readily available finite element codes with the addition of a small subroutine to determine which MPCs to release. Moreover, it retains the advantage of intrinsic CZM without having too much of the added compliance problem and behaves like extrinsic CZM without the complexity of the data structure for adaptive insertion. In Ref. [33], the authors applied the selective activation strategy to arbitrary crack propagation problems of isotropic materials and showed that the strategy could alleviate the added compliance problem significantly and reduce the computation time as well.

The present study extended the selective activation strategy to the fracture problem of laminated composite materials. Because fracture occurs under a combination of failure modes such as fiber fracture, matrix cracking, and delamination, finite bulk element meshes were generated in such a way that cohesive elements could be inserted accounting for possible fracture modes. The inserted cohesive elements were deactivated before analysis by tying the duplicated cohesive nodes, which were selectively activated only when an impending failure was predicted during analysis by releasing the tying constraints on the cohesive nodes. The selective activation strategy was applied to solve the composite fracture problems of double cantilever beam (DCB), L-shaped laminate, and notched laminate specimen configurations. In the following, the insertion, deactivation, and activation of cohesive elements are described in detail. Then, the analysis results are compared to those of conventional CZM for verification. Next, the effect of release condition is carefully examined, as well as the computational efficiency of the present strategy.

2. Analysis: selective activation of intrinsic cohesive elements

To accurately predict the progressive failure behavior of composite materials using intrinsic CZM, prior to analysis, one must insert cohesive elements between all bulk elements in the region where failure is expected to develop. In the analysis, only a small number of cohesive elements in and near the failure region actually take part in the process of failure simulation, whereas most cohesive elements stay in the elastic region of the TSL throughout the analysis, which is wasteful as it causes an added compliance effect and a huge increase of degrees of freedom (DOFs) in computational models. The above problem can be alleviated by deactivating the inserted cohesive elements before analysis and then selectively activating them when and where needed. This can be accomplished by using a controllable user-defined MPCs.

The deactivation-selective activation of cohesive elements is illustrated in Fig. 2. The strategy proceeds in four steps as listed below:

Step 1. Generate the bulk element mesh.
Step 2. Insert the cohesive elements between all bulk elements to generate a 'full' CZM mesh.
Step 3. Deactivate all cohesive elements by tying the duplicate cohesive nodes by using MPCs prior to analysis.
Step 4. Selectively activate the cohesive elements as needed during analysis by releasing the MPCs in the region where an impending failure is predicted.

Here, the 'full' CZM mesh consists of 8 hexahedron bulk elements and 12 cohesive zone elements (CZEs). Cohesive elements have practically "zero" thickness, although they are drawn as having a finite thickness for illustration purposes. The total number of nodes of the CZM mesh is increased to 64 from 27 of the bulk element-only mesh because a large number of duplicate nodes are generated by the insertion of cohesive elements. These duplicate nodes are tied in Step 3 by applying MPCs, leaving a unique node at each nodal location. Then, the

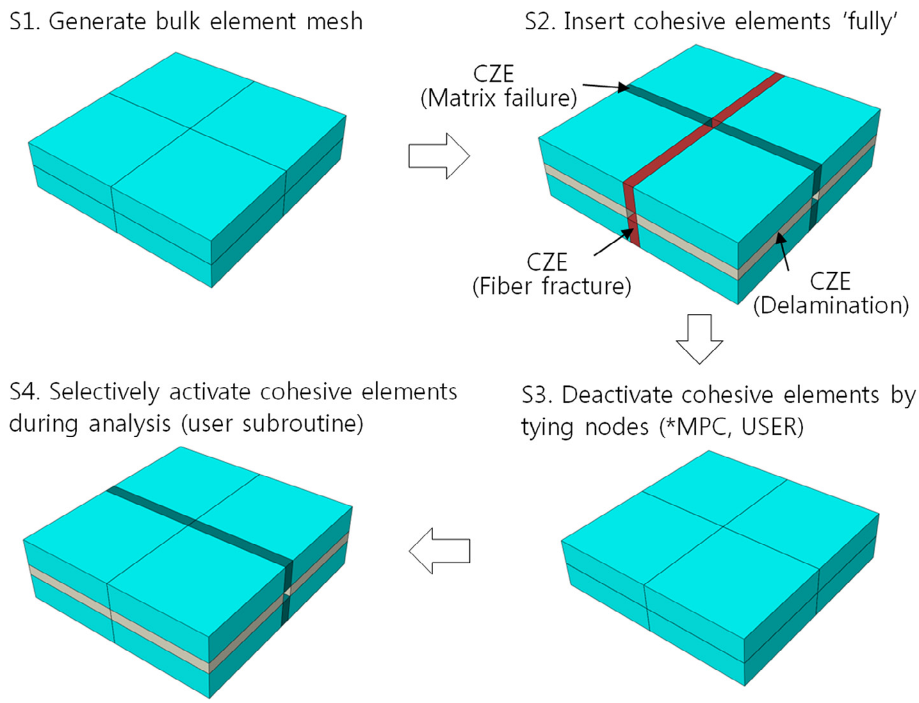

Fig. 2. Schematic of the deactivation and activation of cohesive elements using controllable MPCs.

total number of active nodes becomes the same as that of the bulk element-only mesh, after which the analysis starts and continues until the MPCs are released. In Step 4, the MPCs for locations where failure is predicted to initiate during analysis are selectively released and then the corresponding cohesive elements become activated. In Step 4 of the figure, as an example, the cohesive elements for matrix failure and delamination are illustrated as active, whereas those for fiber fracture are still dormant.

The order of MPC equations can be determined by considering the possible sequence of fracture. In laminated composites, typical failure modes include fiber failure, matrix failure, and delamination. (If other failure modes are present, the procedure can be easily applied to them.) Although failure can develop in different sequences depending on each problem, one may assume that either matrix failure or delamination is initiated first and fiber failure occurs last. In this study, MPCs were defined for cohesive nodes, assuming that the failure occurred in the sequence of delamination, matrix failure, and fiber fracture. To reflect this, we defined MPC equations in reverse order. As shown in Fig. 3, MPCs are hierarchically defined in three levels as follows:

Level 1: Fiber fracture CZE nodes (Eqs. (1a)–(1d)),
Level 2: Matrix failure CZE nodes (Eqs. (2a)–(2b)), and
Level 3: Delamination CZE nodes (Eq. (3)).

At the circled location in Fig. 3, eight duplicate nodes are generated, which are parts of eight 'zero' thickness cohesive elements. Nodes 1–8 are in the same location but are plotted as separate for illustration purposes. Before the start of the analysis, the seven duplicated nodes 2–8 are tied to node 1 by applying seven MPC equations. First, the MPCs are applied to the fiber fracture CZE nodes, enslaving four out of eight nodes, which are expressed in Eqs. (1a)–(1d):

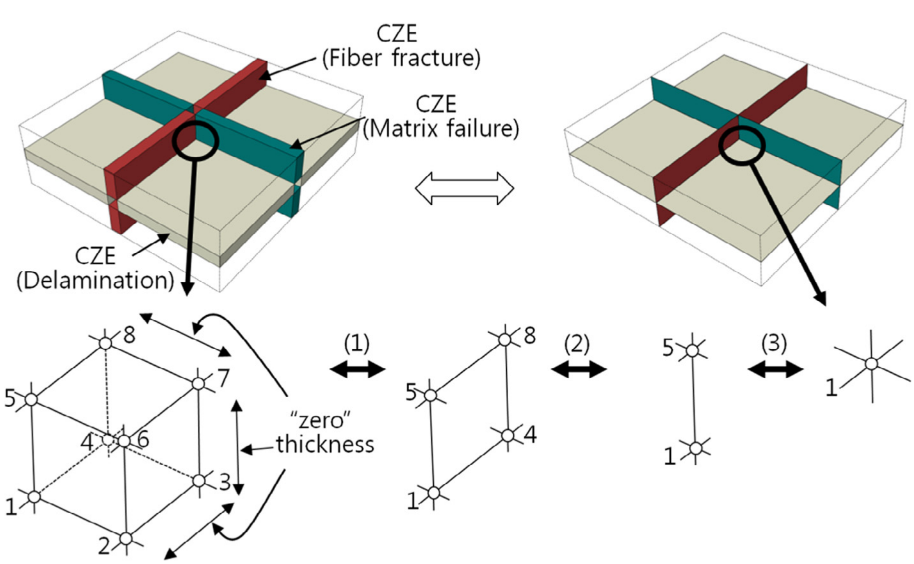

Fig. 3. Application and release of MPCs. (Nodes 1–8 are in the same location but are plotted as separate for illustration purpose.)

$$u_i^1 - u_i^2 = 0 \tag{1a}$$

$$u_i^4 - u_i^3 = 0 \tag{1b}$$

$$u_i^5 - u_i^6 = 0 \tag{1c}$$

$$u_i^8 - u_i^7 = 0 \tag{1d}$$

Here, the subscript i indicates the displacement component (i = 1, 2, 3). Next, two nodes are further enslaved by applying MPCs to the matrix failure CZE nodes as shown in Eqs. (2a)–(2b).

$$u_i^1 - u_i^4 = 0 \tag{2a}$$

$$u_i^5 - u_i^8 = 0 \tag{2b}$$

Finally, the MPC application to the delamination CZE nodes in Eq. (3) ties two nodes, leaving only one unique node.

$$u_i^1 - u_i^5 = 0 \tag{3}$$

At this time, node 1 is the only active node at this location and the total number of active nodes of the mesh becomes the same as that of the bulk element-only mesh. The cohesive elements are still there but dormant, as no deformation is allowed in the cohesive elements by the MPCs. Once the analysis is started, the initial solution is the same as the solution with the bulk element-only mesh and, thus, there is no added compliance problem.

The MPCs are selectively released during analysis when a certain failure is predicted to occur at the corresponding node location. If failure occurs in the same order as assumed for a location, MPC Eq. (3) is released first, then Eqs. (2a)–(2b), and finally Eqs. (1a)–(1d). However, there are possibilities that failure may occur in a different order. For example, consider a case where fiber fracture precedes both matrix failure and delamination. Because of the assumed hierarchy of the MPC equation definition, some of MPC equations of fiber fracture cannot be released because the master nodes of the corresponding MPC equations are not active. That is, the release of four MPC equations (Eqs. (1a)–(1d)) is needed; however, MPC Eqs. (1b), (1c), and (1d) cannot be released because master nodes 4, 5, and 8 do not exist in the model at this time, unless the higher level MPCs are released first.

To resolve this, we need to define linkages between MPC equations, and for the release of any MPC equation, all the linked higher level equations are released simultaneously. In the current example, as summarized in Table 1, Eq. (1a) has no linkage, and thus, it is released independently. However, Eqs. (1b) and (1c) are released after linked Eqs. 2(a) and (3) are released at the same time, respectively. The release of Eq. (1d) requires the release of linked Eqs. 2(b) and (3).

Determining when and where to release MPCs requires a certain criterion. In extrinsic CZM, a cohesive element is inserted and activated if the inter-element traction extrapolated from the connected bulk elements reaches a critical value (e.g., T_{max}). The same idea can be applied to the present method, too; however, a much simpler but more flexible way may be employed. Unlike in extrinsic CZM, intrinsic cohesive elements do not have to be activated when the calculated traction reaches the critical value exactly. They can be activated anywhere when traction is between zero and T_{max}.

Table 1
Definition order and linkage of MPC equations.

MPC equation	Master node	Slave node	Failure mode	Definition hierarchy	Linkage
1(a)	1	2	Fiber fracture	Level 1	–
1(b)	4	3			2(a)
1(c)	5	6			3
1(d)	8	7			2(b)
2(a)	1	4	Matrix failure	Level 2	–
2(b)	5	8			3
3	1	5	Delamination	Level 3	–

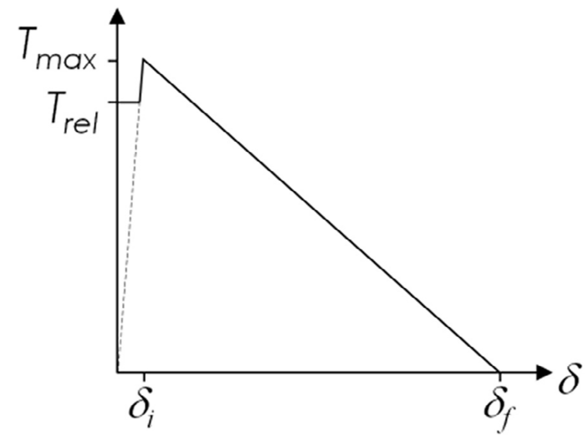

Fig. 4. Modified intrinsic TSL. (The cohesive element is activated at T_{rel}.)

This can be understood easily from Fig. 4, which shows the TSL of the selectively activated cohesive element. Here, δ_i and δ_f indicate the failure initiation displacement corresponding to T_{max} and the failure completion displacements, respectively, and T_{rel} is the MPC release traction which is a controllable value in the range of

$$0 \le T_{rel} \le T_{max} \tag{4}$$

The TSL is modified from the conventional intrinsic one such that it is initially rigid until the traction is less than or equal to T_{rel}, after which it follows the conventional TSL. If one sets $T_{rel} = 0$, the conventional intrinsic CZM is recovered, and if $T_{rel} = T_{max}$, a quasi-extrinsic CZM behavior is obtained. One may set $T_{rel} = T_{max}$ and choose to activate the cohesive element just when needed. However, there is no guarantee that the calculated inter-element traction value will be accurate and there is a possibility of over-constraining.

In the present study, the value of T_{rel} was selected to be slightly less than T_{max}. That is, the cohesive elements were activated slightly earlier than needed. This was thought to be a good strategy to avoid the numerical burden of accurately calculating inter-element traction values. One can even use stress values instead of traction values to determine when to release the MPCs. In this case, one may directly use nodal point stress values (maximum stress criterion) or failure indices calculated by a more sophisticated failure criterion.

When a failure criterion is used instead of traction values, MPCs are released when the failure index (ϕ_i) is equal to the pre-set MPC-release failure index (ϕ_i^r), i.e.,

$$\phi_i = \phi_i^r \tag{5}$$

where the subscript i indicates the failure modes: 1 for fiber fracture, 2 for matrix cracking, and 3 for delamination. Thus the pre-setting of ϕ_i^r can be controlled separately for each failure mode. Like in Eq. (4), one can set ϕ_i^r to be any number between 0 and 1, with 1 indicating failure. In the preliminary analysis, it was found that, in general, the values of ϕ_i^r = 0.9–0.95 (which were approximately equivalent to T_{rel} values of 90–95% of T_{max}) were high enough to delay the release of MPCs and thus delay the activation of cohesive elements, while they were released before the onset of failure.

It is well known that there is no single failure criterion that can predict all failure modes accurately. However, as explained above, selecting a failure criterion for the present purpose is not so significant a concern because the failure criterion is just used to determine when to release the MPCs, not to determine the actual failure initiation. In the preliminary analysis, several composite failure criteria were tested, and it was found that the difference in the results was not significant. The results presented in this paper were produced by using Hashin's failure criteria [34] for the intra-ply failure (Eqs. (6)–(9)) and Chang-Chang criteria [35] for the delamination (Eq. (10)).

Tensile fiber mode ($\sigma_{11} > 0$)

$$\left(\frac{\sigma_{11}}{X_T}\right)^2 + \frac{\sigma_{12}^2 + \sigma_{13}^2}{S_{12}^2} = 1 \tag{6}$$

Compressive fiber mode ($\sigma_{11} < 0$)

$$\frac{-\sigma_{11}}{X_C} = 1 \tag{7}$$

Tensile matrix mode ($\sigma_{22} + \sigma_{33} > 0$)

$$\left(\frac{\sigma_{22} + \sigma_{33}}{Y_T}\right)^2 + \frac{\sigma_{12}^2 + \sigma_{13}^2}{S_{12}^2} + \frac{\sigma_{23}^2 - \sigma_{22}\sigma_{33}}{S_{23}^2} = 1 \tag{8}$$

Compressive matrix mode ($\sigma_{22} + \sigma_{33} < 0$)

$$\left[\left(\frac{Y_C}{2S_{23}}\right)^2 - 1\right]\frac{\sigma_{22} + \sigma_{33}}{Y_C} + \left(\frac{\sigma_{22} + \sigma_{33}}{2S_{23}}\right)^2 + \frac{\sigma_{23}^2 - \sigma_{22}\sigma_{33}}{S_{23}^2} + \frac{\sigma_{12}^2 + \sigma_{13}^2}{S_{12}^2} = 1 \tag{9}$$

Delamination

$$\left(\frac{\sigma_{33}}{Z_T}\right)^2 + \left(\frac{\sigma_{23}}{S_{23}}\right)^2 + \left(\frac{\sigma_{13}}{S_{13}}\right)^2 = 1 \tag{10}$$

where X_T, X_C, Y_T, Y_C, Z_T and Z_C denote the normal tensile and compressive strengths in the material 1, 2, and 3 directions, respectively, and S denotes the shear strength. The directional components are indicated by the subscripts 1, 2 and 3.

The strategy of selective activation of cohesive elements was implemented in ABAQUS using a user subroutine (MPC.for). At the end of the converged iterations, the nodal stress results of the bulk elements were obtained by accessing the integration point stresses using the utility subroutine GETVRM.for and then extrapolating them to nodal values.

With the present method, computational costs can be reduced because, until failure initiation, the number of active DOFs is the same as that of the bulk element-only mesh. Even after failure initiation, the number of active DOFs increases only slightly because the failure region where the MPCs are released is limited to a small portion of the model for most cases.

It should be noted that element calculations for dormant cohesive elements are not necessary; they were performed in this study though because, currently, the method is implemented as a user subroutine. This unnecessary computation can be avoided when the method is fully incorporated with the finite element codes, which should further reduce the computational cost.

3. Results and discussion

3.1. Application to DCB configuration

The selective activation strategy was first applied to a double cantilever beam (DCB) specimen taken out from Ref. [36]. The length (L), the width (W), and the total thickness (t) of the beam were 100 mm, 20 mm, and 3 mm, respectively, as shown in Fig. 5. The beam was made of 24 carbon/epoxy plies having a 0° orientation angle and a 30-mm initial delamination (a_0). The material properties are given in Table 2. In this case, a limited number of cohesive elements need to be inserted only along the centerline, and, therefore, there is little added compliance problem; however, the configuration was selected to verify whether the present selective activation strategy was working properly.

A three-dimensional (3D) mesh was generated using solid elements

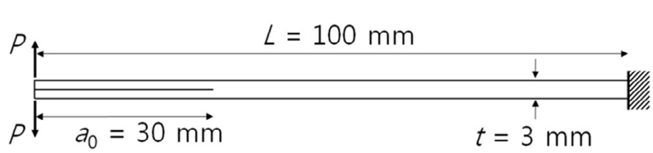

Fig. 5. DCB configuration [36].

Table 2
Elastic and cohesive properties for DCB specimen [36].

Composite					Interface	
E_{11} (GPa)	E_{22} (GPa)	G_{12} (GPa)	ν_{12}	ν_{23}	G_{IC} (N/mm)	T_1 (MPa)
135.3	9.0	5.2	0.24	0.46	0.28	57.0

(C3D8) with cohesive elements (COH3D8) inserted along the delamination path. Although a two-dimensional (2D) plane strain modeling can solve this problem, as was done in Ref. [36], a 3D modeling was performed herein to demonstrate the 3D capability of the developed selective activation strategy. Element size (h^e) was determined by first estimating the cohesive zone size (l_{cz}) and then placing an enough number of elements inside it [15]. The element size used in the analysis was 0.125 mm. The configuration was modeled using one element in the lateral direction, and the lateral displacements were constrained at the front and back surfaces to simulate the plane strain condition. The initial cohesive stiffness used was $K = 9 \times 10^3$ GPa/mm, and a small amount of artificial damping was applied to stabilize the solution procedure. A pair of opening displacement loads was applied at the left end to have mode I delamination propagation.

A conventional CZM analysis was done first, and then a CZM analysis with the selective activation strategy via a user MPC subroutine was performed. Fig. 6 shows a comparison between the load-displacement curves obtained by the conventional CZM (CCZM) and by the user MPC-controlled CZM (MCZM) of the selective activation strategy. Here, the MCZM result was obtained with the MPC release value for the delamination $\phi_3^r = 0.5$ and 0.75. The MCZM result agreed almost exactly with that by CCZM, indicating that the user MPC method produced a result that was basically the same that produced by the conventional CZM. The result also very closely matched that obtained by Ref. [36], with indistinguishable difference.

3.2. Application to the delamination problem of an L-shaped laminated composite

Next, the present approach was applied to an L-shaped curved laminated composite with multiple delamination failures. As shown Fig. 7, the curved part had an inner radius of 15 mm connected with a 125-mm straight upper arm and a 75-mm lower leg. The thickness and the width were 10 mm and 50 mm, respectively. The laminate was fixed at the lower end, and the vertical load was applied at the upper arm by a steel bar at 50 mm from the right end, which produced an opening

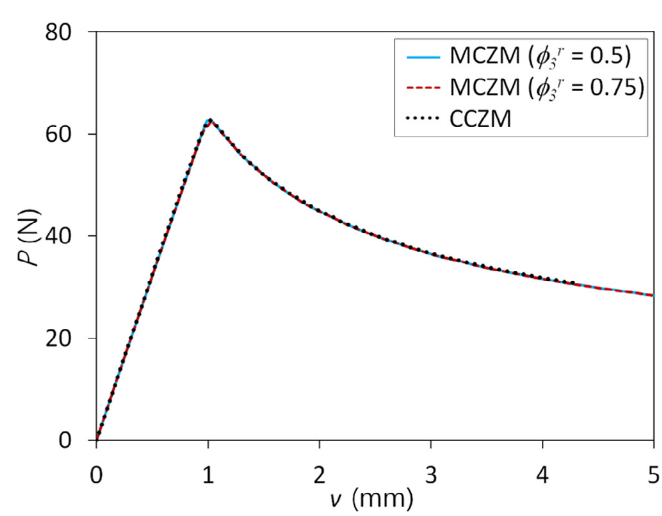

Fig. 6. Comparison between the load-displacement curves for the DCB configuration.

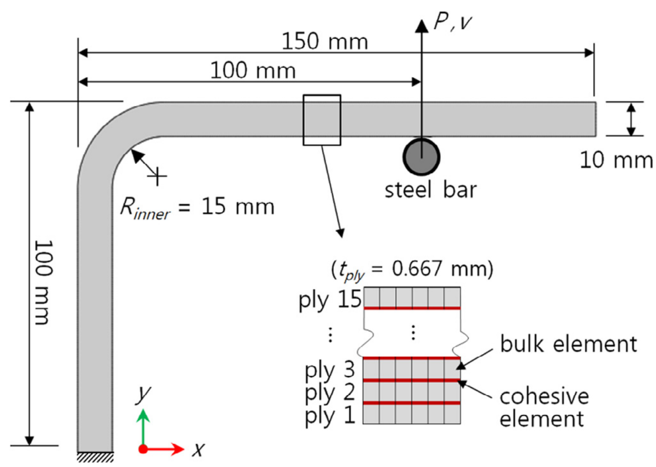

Fig. 7. Configuration of the L-shaped laminated composite.

Table 3
Material properties of the L-shaped laminated composite.

(a) Elastic

E_{11} (GPa)	E_{22} (GPa)	E_{33} (GPa)	ν_{12}	ν_{13}	ν_{23}	G_{12} (GPa)	G_{13} (GPa)	G_{23} (GPa)
33	2.5	20	0.3	0.3	0.3	2.2	5	2

(b) Cohesive

T_1 (MPa)	T_2 (GPa)	G_{IC} (N/mm)	G_{IIC} (N/mm)	η (B-K)
15	77	0.6	1.25	1.8

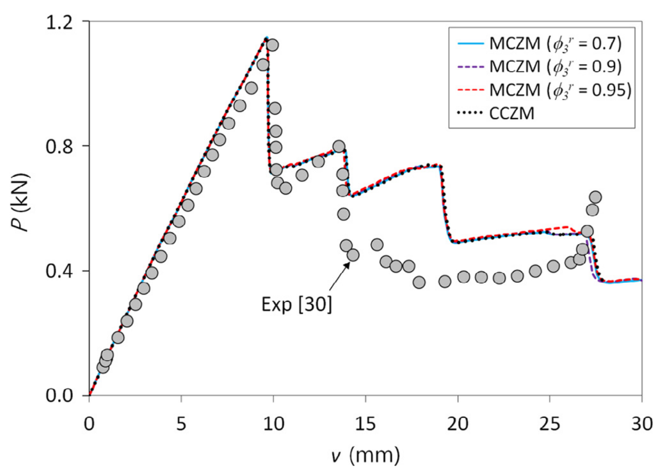

Fig. 8. Load-displacement curves of the L-shaped laminated composite.

deformation of the curved part. The laminate consisted of 15 triaxially braided glass/epoxy composite plies, the elastic and cohesive properties of which are given in Table 3 [37]. Here, the material axes (1, 2, and 3) were the length, thickness, and width directions of the laminate, respectively.

The element size was determined again by first estimating the cohesive zone length using the properties given in Table 3 and placing an enough number of elements within. The mesh was generated from one slab of the 3D elements, with the plane strain conditions applied at the front and back surfaces. The mesh contained 13,770 solid elements (C3D8) and 4,284 cohesive elements (COH3D8) inserted in every ply interface along the entire length of the laminate part, and 262 solid elements (C3D8/C3D6) for the steel bar. (Cohesive elements are inserted between all interfaces along the entire length.) A vertical

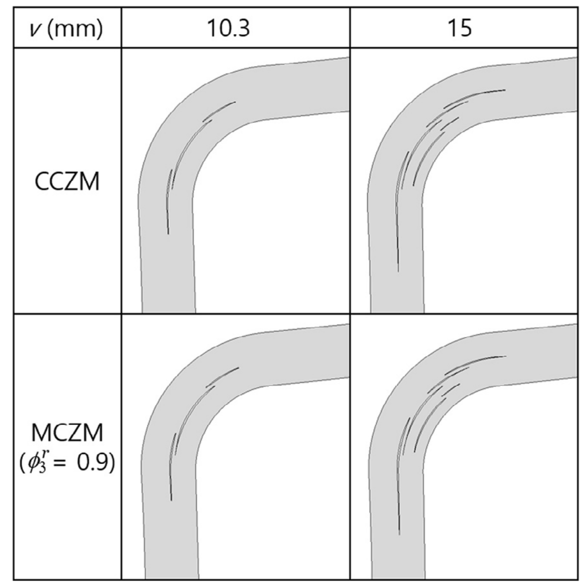

Fig. 9. Comparison of the delamination shape (deformation scale factor = 1).

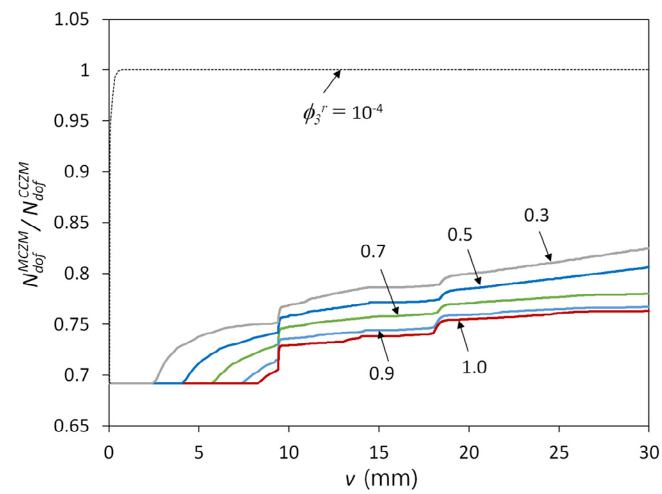

Fig. 10. History of the number of active DOFs of the L-shaped laminated composite for various MPC release failure indexes.

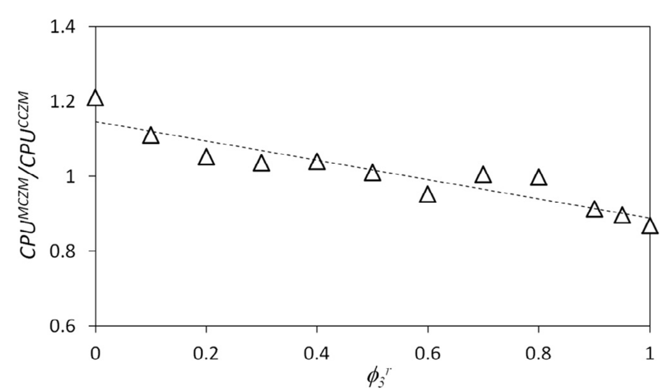

Fig. 11. Variation of normalized CPU time versus MPC release failure index of L-shape laminated composite.

displacement load was applied to the steel bar; it was transferred to the laminate through frictionless surface-to-surface contact. The quadratic stress criterion (QUADS) and an energy-based criterion were used with the Benzeggagh-Kenane (BK) law [38] for the mixed-mode failure

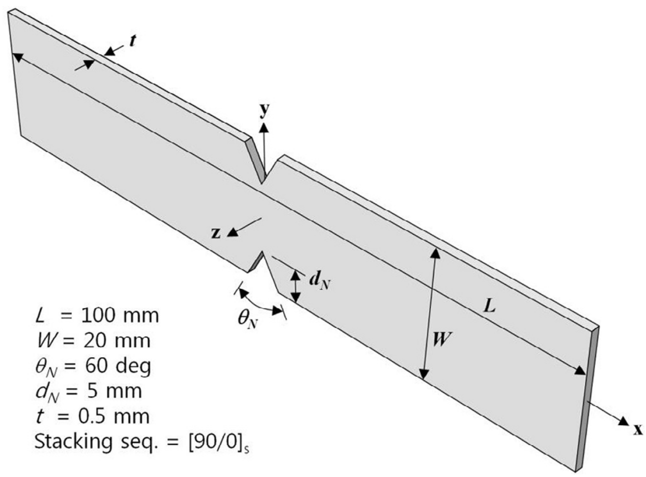

Fig. 12. Configuration of the double-edge notched tensile cross-ply laminate.

Table 4
Material properties of the double-edge notched cross-ply laminate [4].

(a) Elastic					
E_{11} (GPa)	$E_{22} = E_{33}$ (GPa)	$\nu_{12} = \nu_{13}$	ν_{23}	$G_{12} = G_{13}$ (GPa)	G_{23} (GPa)
43.9	15.4	0.3	0.4	4.34	3.2

(b) Cohesive					
Failure mode	T_1 (MPa)	T_2 (MPa)	G_{IC} (N/mm)	G_{IIC} (N/mm)	Mixed-mode power
Fiber fracture	1200	–	50	–	1
Matrix failure	40	75	0.25	1.0	2
Delamination	40	75	0.25	1.0	1.8 (B-K)

initiation and failure evolution, respectively.

Fig. 8 shows a comparison between the load-displacement curves of the L-shaped laminated composite. The MCZM results with different MPC release values (ϕ_3^r) agreed well with the CCZM result, with little difference, which indicates again that the MPC-controlled selective activation strategy was able to produce a result that matched the result by the conventional CZM. Compared to the experiment result, both the MCZM and the CCZM results correctly predicted the elastic response, the maximum load, and the first and the second major load drops, indicating that the CZM modeling was done accurately. The shape of the delamination is compared in Fig. 9 for various applied load levels. In the figure, one can see that the delamination development predicted by the MCZM with ϕ_3^r = 0.9 matched with that by the CCZM very accurately, indicating again that the MCZM with the selective activation strategy produced results that were as good as those produced by the conventional CZM.

The history of the number of active DOFs (N_{dof}) of the MCZM is plotted in Fig. 10. The N_{dof} values were normalized by the CCZM value, which was 55,632. For the MCZM, the initial N_{dof} was 38,496, which was the same as that of the bulk element-only mesh. When ϕ_3^r was set to zero, N_{dof} increased immediately and became the same as the CCZM value as all MPCs were released right away. For other release values of ϕ_3^r, N_{dof} increased versus the applied displacement as the MPCs were released but remained much smaller. For ϕ_3^r = 0.9, the MCZM analysis was done with N_{dof} of less than 76.3% of the CCZM value.

The reduction in active DOFs translated into a reduction in CPU time. Fig. 11 shows the variation of the normalized CPU time of the MCZM versus the MPC release value. In general, the CPU time showed a steady decrease as the MPC release value increased. In this case, as can be seen in the figure, the savings in CPU time were not significant. This was mainly because the problem size was not big enough. It was thought that the savings in computation time due to the reduction in N_{dof} were cancelled out by the time spent in the user MPC operation (MPC initialization, calculation of the failure index, and determining whether to release the MPCs or not).

3.3. Application to the double-edge notched tensile specimen configuration

In the previous two problems, the effect of added compliance was not significant as cohesive elements were inserted only along a limited number of crack paths. In this section, we discussed the application of the selective activation strategy a double-edge notched cross-ply laminate configuration under tension, as shown in Fig. 12, which had a

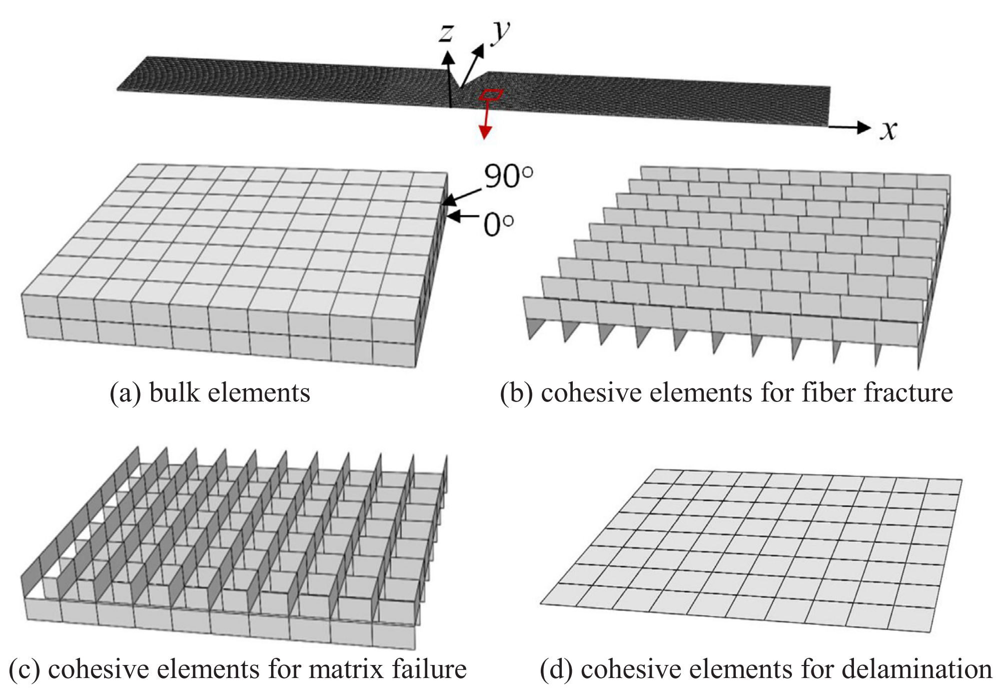

Fig. 13. Finite element mesh with fully inserted cohesive elements for the configuration of the double-edge notched tensile cross-ply laminate.

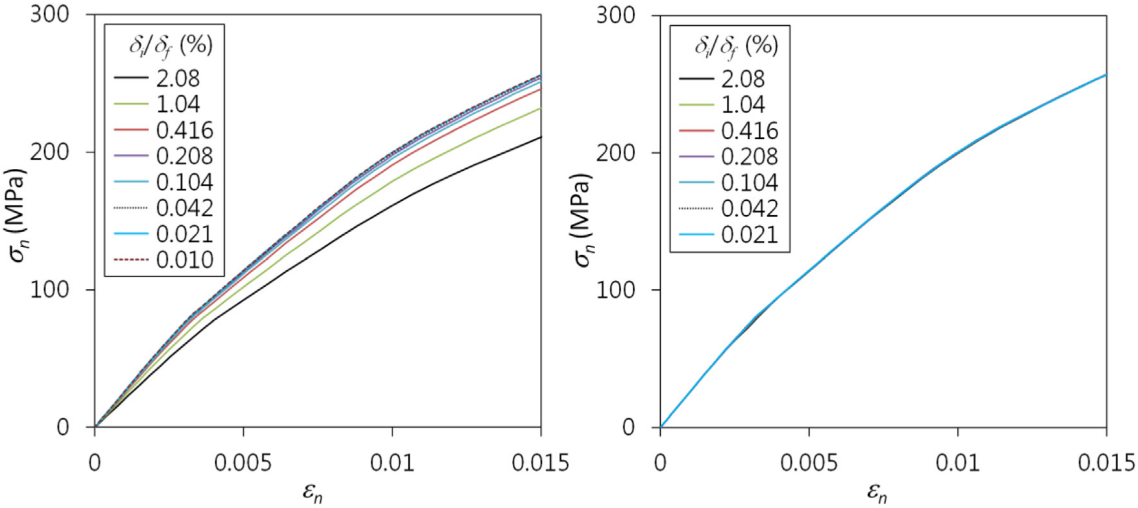

(a) CCZM (b) MCZM ($\phi_1^r = 0.95,\ \phi_2^r = \phi_3^r = 0.9$)

Fig. 14. Effect of added compliance on the nominal stress-strain curve.

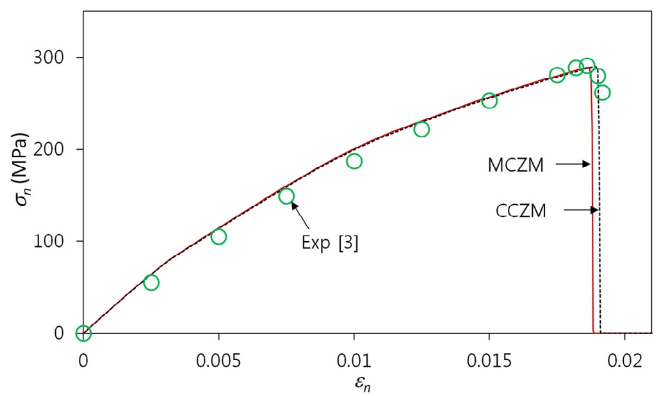

Fig. 15. Comparison of the nominal stress-strain curve ($\delta_i/\delta_f = 0.021\%$, $\phi_1^r =$ 0.95, and $\phi_2^r = \phi_3^r = 0.9$ for the MCZM).

complex combination of matrix cracking, delamination, and fiber fractures. The material properties are listed in Table 4. This problem was studied experimentally and numerically in Refs. [3,4] where CZM was used to model the delamination and the fiber splitting developed from the tip of the notch. Although able to capture the significant part of the failure behavior, the selective consideration of failure modes in Ref. [4] did not completely account for the nonlinear behavior of the development and interaction of failure modes, where a full insertion of cohesive elements is needed to model not only the above but also a large amount of matrix cracking and fiber fracture. In this case, the use of the conventional CZM would have the added compliance issue and cause a huge increase in the size of the computation, and the selectively activated MCZM was thought to be a more efficient option.

In the finite element modeling, one-fourth portion ($-L/2 \le x \le L/2$, $0 \le y \le W/2$, and $0 \le z \le t/2$) was discretized, and y- and z-symmetry conditions were applied at $y = 0$ and $z = 0$ planes, respectively. The finite element mesh was modeled using solid elements (C3D8/C3D6) and cohesive elements (COH3D8/COH3D6). As shown in the zoomed-in view of Fig. 13, the cohesive elements were inserted between all bulk elements and then classified according to the failure modes. The element size used was $h^e = 0.25$ mm, which corresponded to placing 3.1 elements in the estimated cohesive zone length (l_{cz}). (A preliminary analysis with $h^e = 0.125$ mm was performed; however, the difference in the results was not significant.) For this mesh, MPCs were applied hierarchically and the linkages between MPCs were defined. The number of bulk elements was 18,780; that of cohesive elements for fiber fracture, matrix failure, and delamination was 18,464, 18,464, and 9,390, respectively; and that of MPCs was 121,185.

For the cohesive analysis settings, quadratic failure initiation was used for the matrix failure and delamination, whereas maximum stress failure initiation was used for the fiber fracture. For the mixed mode-behavior, a power law ($p = 2$) and the B-K law ($\eta = 1.8$) [38] were used for the matrix and delamination failures, respectively, whereas no mode-mixing was assumed for the fiber fracture.

Fig. 14 shows the effect of added compliance on the nominal stress (σ_n) - strain (ε_n) curves for the CCZM results for various initial cohesive stiffness values. (Here, the ratio between failure initiation and completion displacements was used instead of K for the initial stiffness.) As can be seen in the figure, the CCZM result had a significantly softened response when $\delta_i/\delta_f = 2\%$. In this case, the nominal stress value at 1% nominal strain was 18.9% smaller than the converged one. The CCZM results gradually converged as δ_i/δ_f decreased (i.e., the initial stiffness increased); however, δ_i/δ_f had to be reduced to 0.042% to have a convergence with less than 1% difference in the stress value at 1% strain. In contrast, the MCZM results showed no distinguishable

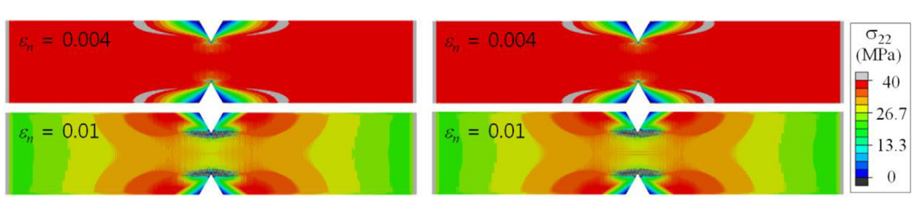

(a) CCZM (b) MCZM

Fig. 16. Comparison of the σ_{22} stress in the 90° ply.

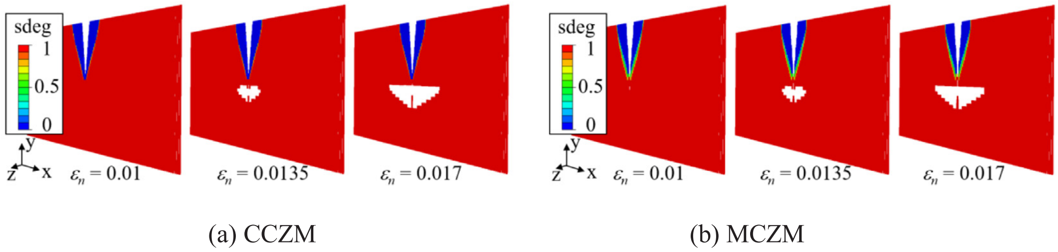

Fig. 17. Comparison of the damage state variable (SDEG) of matrix failure cohesive elements in the 90° ply. (The upper half portion is plotted.)

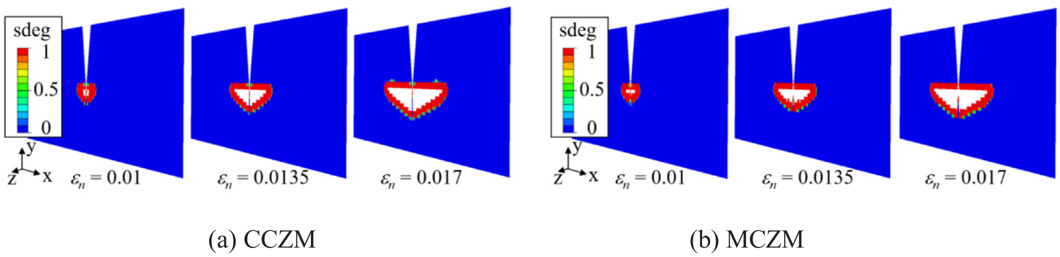

Fig. 18. Comparison of the damage state variable (SDEG) of delamination cohesive elements. (The upper half portion is plotted.)

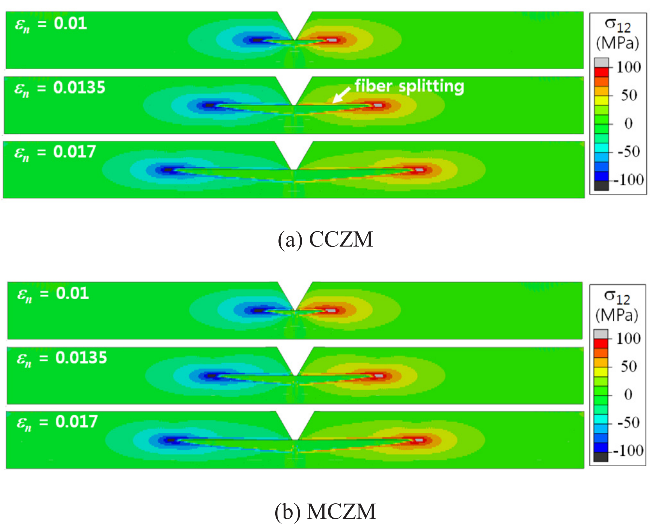

Fig. 19. Comparison of the σ_{12} stress in the 0° ply. (The upper half portion is plotted.)

difference for various δ_i/δ_f values. All curves matched with each other almost exactly indicating no added compliance for the MCZM.

The complete nominal stress-strain curves are compared in Fig. 15. The predicted stress-strain curves by the CCZM and the MCZM with $\delta_i/\delta_f = 0.021\%$ matched very well with each other, whereas the CCZM result still showed a slight effect of added compliance. These also agreed well with the experimental result given in Ref. [3], indicating that the finite element modeling was done accurately.

Figs. 16 and 17 show the comparison of the σ_{22} stress and the damage state variable (SDEG) at the top surface of the 90° ply, respectively, at different applied nominal strain levels, and Fig. 18 shows the delamination damage state variable. (The top view of the full specimen is shown in Fig. 16, while the inclined views of the half part are shown in Figs. 17 and 18.) In the figures, the development histories of the 90° ply matrix damage and the inter-ply delamination calculated by the CCZM and the MCZM matched very accurately. These figures indicate that the MCZM produced a failure progression history that was as good as the CCZM. In Fig. 16, the matrix failure process of the 90° ply started at around $\varepsilon_n = 0.002$ near the notch tip, which grew as the nominal strain increased and engulfed the entire 90° ply at $\varepsilon_n = 0.004$. This resulted in the first slope change in the stress-strain curve shown in Fig. 15. The matrix failure process in the 90° ply occurred gradually as it was attached to the 0° ply, which carried a major portion of the load. As the applied nominal strain further increased, the matrix failure process continued and σ_{22} decreased. The final matrix failure started to occur at the region near the notch tip when the applied nominal strain was larger than 0.01 as can be seen in Fig. 17. The fully failed cohesive elements were deleted and marked as white areas in the figure. At this load level, the inter-ply delamination also started from the notch tip region and grew mainly in the loading direction as shown in Fig. 18. The location of deleted cohesive elements of matrix failure coincided with those of delamination, indicating that the full matrix failure of the 90° ply occurred after the failing part was detached from the adjacent 0° ply. Both the shape and the propagation distance of the predicted

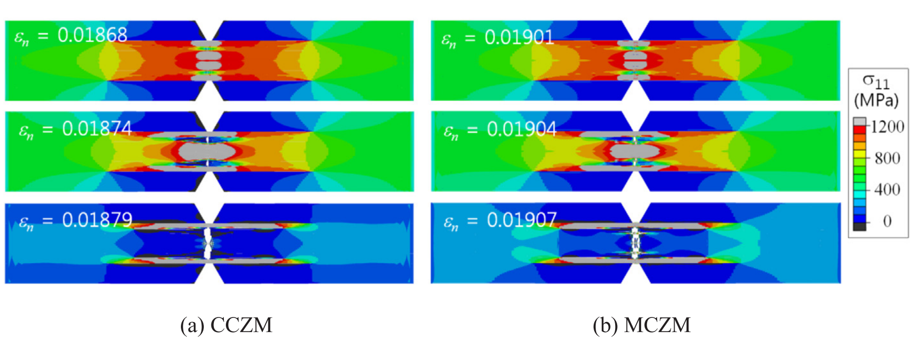

Fig. 20. Comparison of fiber failure progression in the 0° ply.

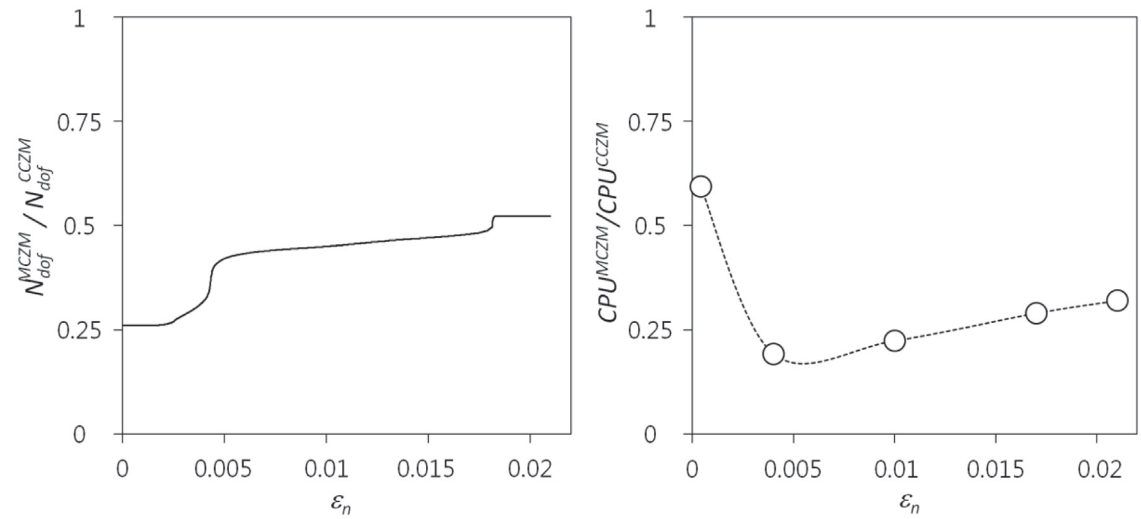

(a) N_{dof} (b) CPU time

Fig. 21. History of the normalized active number of DOFs and the CPU time for the configuration of the double-edge notched tensile cross-ply laminate.

matrix failure and delamination by the CCZM and the MCZM matched closely.

Fig. 19 shows the comparison of the in-plane shear stress (σ_{12}) history of the 0° ply. The two stress histories predicted by the CCZM and the MCZM matched accurately with each other. In the figure, the matrix cracking (fiber splitting) developed from the notch tip and propagated in the horizontal direction in the 0° ply. (The horizontal line growing from the notch tip marks the fully failed and thus deleted matrix failure cohesive elements.) The propagation length of the fiber splitting and the enveloping line of high σ_{12} stress corresponded closely to the extent of the delaminated region shown in Fig. 19, indicating that the fiber splitting in the 0° ply interacted with other intra- inter-laminar stresses and affected in producing the delamination and the final matrix failure of the 90° ply in Figs. 17 and 18.

The predicted fiber failure shape is compared in Fig. 20. The fiber failure progression pattern by the MCZM agreed reasonably well with that by the CCZM. The fiber failure occurred within a very small increase in the applied nominal strain. In both cases, the fiber failure was predicted not to start at the notch tip of the initial geometry (which was no longer the stress concentrating notch tip anymore due to the delamination and the fiber splitting). Instead, it started near the current delamination/matrix failure tip region. The fiber failure then propagated vertically resulting in the final failure.

The history of active number of DOFs (N_{dof}) and the CPU time of the MCZM is plotted in Fig. 21. For these, the parameters used were the same as those in Fig. 15. The MCZM analysis started with about 25% N_{dof} compared to that by the CCZM. Between $\varepsilon_n = 0.002$ and 0.005, matrix failure occurred in the 90° ply and resulted in a steep increase in N_{dof} of the MCZM. After that, N_{dof} increased slowly owing to the steady growth of delamination. Then, a sharp increase occurred at around $\varepsilon_n = 0.018$, which corresponded to the fiber fracture in the 0° ply. The final N_{dof} of the MCZM was 52.2% of that of the CCZM. The reduction in N_{dof} translated into a reduction in CPU time. As can be seen in Fig. 21(b), the normalized CPU time was approximately 56% at the beginning owing to the initialization of the MCZM analysis, but quickly decreased to a 25% level. It then increased gradually, corresponding to the increase in N_{dof}; however, the MCZM analysis was completed in less than 32% of the time by the CCZM analysis.

It should be noted that MCZM requires an additional preparation in the model generation stage to tie the duplicate cohesive nodes and to define the node linkage for the failure hierarchy, while the procedures for the finite element mesh generation and the insertion of cohesive elements are the same for both CCZM and MCZM. A small in-house code was generated to do the tie and the linkage definition. Using the code, the additional preparation takes seconds for small meshes and a few minutes for large meshes with the number of elements in the order of 10^5. The additional preparation time was only a small fraction of the analysis time for the notched-edge notched tensile specimen configuration and the saving in CPU was still significant even with the added preparation time. The saving is expected to become much more significant for realistic engineering problems with increased number of elements.

4. Conclusion

In this study, an efficient selective activation of cohesive elements using controllable user-defined MPC was implemented for fracture analysis of laminated composites. With this method, finite element meshes were generated with the cohesive elements fully inserted. Then the cohesive elements were deactivated by tying the duplicated cohesive nodes by the MPC, which were selectively activated during analysis by releasing the MPCs. For application to the fracture analysis of laminated composites, a strategy for systematic definition and release of MPCs considering the composite failure mode was developed. When applied to fracture analysis problems, the selective activation method was found to produce matched results compared to those by the conventional CZM. The added compliance problem was alleviated, and the required computer resources (memory and CPU time) were reduced significantly.

Acknowledgement

This work was supported by Defense Acquisition Program of Republic of Korea through Dual Use Technology Development Project 2017 (14-CM-MP-10).

Appendix A. Supplementary material

Supplementary data to this article can be found online at https://doi.org/10.1016/j.compstruct.2018.11.055.

References

[1] Davila CG, Camanho PP, Rose CA. Failure criteria for FRP laminates. J Compos

Mater 2005;39(4):323–45. https://doi.org/10.1177/0021998305046452.

[2] Kortschot MT, Beaumont PWR. Damage mechanics of composite materials I: measurements of damage strength. Compos Sci Technol 1990;39(4):289–301. https://doi.org/10.1016/0266-3538(90)90077-I.

[3] Hallet SR, Wisnom MR. Experimental investigation of progressive damage and the effect of layup in notched tensile tests. J Compos Mater 2005;40(2):119–41. https://doi.org/10.1177/0021998305053504.

[4] Hallet SR, Wisnom MR. Numerical investigation of progressive damage and the effect of layup in notched tensile tests. J Compos Mater 2006;40(14):1229–45. https://doi.org/10.1177/0021998305057432.

[5] Higuchi R, Okabe T, Nagashima T. Numerical simulation of progressive damage and failure in composite laminates using XFEM/CZM coupled approach. Composites: Part A 2017;95:197–207. https://doi.org/10.1016/j.compositesa.2016.12.026.

[6] Krueger R. The virtual crack closure technique: history, approach and applications. Appl Mech Rev 2004;57(2):109–43. https://doi.org/10.1115/1.1595677.

[7] Liu PF, Hou JK, Hu XY, Zhou CL, Liu YL, Zheng JY, et al. Finite element analysis of postbuckling and delamination of composite laminates using virtual crack closure technique. Compos Struct 2011;93:1549–60. https://doi.org/10.1016/j.compstruct.2010.12.006.

[8] Ladeveze P, Le Dantec E. Damage modelling of the elementary ply for laminated composites. Compos Sci Technol 1992;43:257–67. https://doi.org/10.1016/0266-3538(92)90097-M.

[9] Lie S, Nairn JA. The formation and propagation of matrix microcracks in cross-ply laminates during static loading. J Reinf Plast Compos 1992;11(2):158–78. https://doi.org/10.1177/073168449201100204.

[10] Maimi P, Camanho PP, Mayugo JA, Davila CG. A continuum damage model for composite laminates: part II – computational implementation and validation. Mech Mater 2007;39:909–19. https://doi.org/10.1016/j.mechmat.2007.03.006.

[11] Liu PF, Zheng JY. Progressive failure analysis of carbon fiber/epoxy composite laminates using continuum damage mechanics. Mater Sci Eng, A 2008;485:711–7. https://doi.org/10.1016/j.msea.2008.02.023.

[12] Van Der Meer FP, Sluys LJ. Continuum models for the analysis of progressive failure in composite laminates. J Compos Mater 2009;43(20):2131–56. https://doi.org/10.1177/0021998309343054.

[13] Nairn JA, Hammerquist CC, Aimene YE. Numerical implementation of anisotropic damage mechanics. Int J Numer Methods Eng 2017;112(12):1848–68. https://doi.org/10.1002/nme.5585.

[14] Mohammadi B, Rohanifer M, Salimi-Majd D, Farrokhabadi A. Micromechanical prediction of damage due to transverse ply cracking under fatigue loading in composite laminates. J Reinf Plast Compos 2017;36(5):377–95. https://doi.org/10.1177/0731684416676635.

[15] Turon A, Davila CG, Camanho PP, Costa J. An engineering solution for mesh size effects in the simulation of delamination using cohesive zone models. Eng Fract Mech 2007;74(10):1665–82. https://doi.org/10.1016/j.engfracmech.2006.08.025.

[16] Balzani C, Wagner W. An interface element for the simulation of delamination in unidirectional fiber-reinforced composite laminates. Eng Fract Mech 2008;75:2597–615. https://doi.org/10.1016/j.engfracmech.2007.03.013.

[17] Harper PW, Sun L, Hallet SR. A study on the influence of cohesive zone interface element strength parameters on mixed mode behavior. Composites Part A 2012;43(4):722–34. https://doi.org/10.1016/j.compositesa.2011.12.016.

[18] Mohammadi B, Salimi-Majd D. Investigation of delamination and damage due to free edge effects in composite laminates using cohesive interface elements. Eng Solid Mech 2014;2:101–18. https://doi.org/10.5267/j.esm.2014.2.001.

[19] Moslemi M, Khoshravan M. Cohesive zone parameters selection for Mode-I prediction interfacial delamination. J Mech Eng 2015;61:507–16. https://doi.org/10.5545/sv-jme.2015.2521.

[20] Kumar D, Roy R, Kweon J, Choi J. Numerical modeling of combined matrix cracking and delamination in composite laminates using cohesive elements. Appl Compos Mater 2016;23(3):397–419. https://doi.org/10.1007/s10443-015-9465-0.

[21] Huynh DBP, Belytschko T. The extended finite element method for fracture in composite materials. Int J Numer Meth Eng 2009;77(2):214–39. https://doi.org/10.1002/nme.2411.

[22] Radtke FKF, Simone A, Sluys LJ. A partition of unity finite element method for simulating non-linear debonding and matrix failure in thin fiber composites. Int J Numer Methods Eng 2011;86(4–5):453–76. https://doi.org/10.1002/nme.3056.

[23] Iarve EV, Mollenhouer D. Mesh-independent matrix cracking and delamination modeling in advanced composite materials. In: Camanho PP, Hallet SR. Numerical modelling of failure in advanced composite materials; 2017. p. 227–64.

[24] Klein PA, Foulk JW, Chen EP, Wimmer SA, Gao H. Physics-based modeling of brittle fracture: cohesive formulation and the application of meshfree methods. Theor Appl Fract Mech 2001;37:99–166. https://doi.org/10.1016/S0167-8442(01)00091-X.

[25] Paulino GH, Celes W, Espinha R, Zhang Z. A general topology-based framework of adaptive insertion of cohesive elements in finite element meshes. Eng Comput 2008;24:59–78. https://doi.org/10.1007/s00366-007-0069-7.

[26] Pandolfi A, Ortiz M. Solid modeling aspects of three-dimensional fragmentation. Eng Comput 1998;14:287–308. https://doi.org/10.1007/BF01201761.

[27] Papoulia KD, Sam CH, Vavasis SA. Time continuity in cohesive finite element modeling. Int J Numer Methods Eng 2003;58:679–701. https://doi.org/10.1002/nme.778.

[28] Li X, Binienda WK, Goldberg RK. Finite element model for failure study of two-dimensional triaxially braided composite. NASA/TM-2010-216372.

[29] Qu P, Sun X, Guan X, Mu Y, Jia Y. Effect of interlaminar toughness on the low-velocity impact damage in composite laminates. Polym Compos 2016;37(4):1085–92. https://doi.org/10.1002/pc.23270.

[30] Vigueras G, Sket F, Samaniego C, Wu L, Noels L, Tjahjanto D, et al. An XFEM/CZM implementation for massively parallel simulations of composite fracture. Compos Struct 2015;125:542–57. https://doi.org/10.1016/j.compstruct.2015.01.053.

[31] Wu L, Tjahjanto D, Becker G, Makradi A, Jerusalem A, Noels L. A micro-meso-model of intra-laminar fracture in fiber-reinforced composites based on a discontinuous Galerskin/cohesive zone method. Eng Fract Mech 2013;104:162–83. https://doi.org/10.1016/j.engfracmech.2013.03.018.

[32] Kubair DV, Geubelle PH. Comparative analysis of extrinsic and intrinsic cohesive models of dynamic fracture. Int J Solids Struct 2003;40:3853–68. https://doi.org/10.1016/S0020-7683(03)00171-9.

[33] Woo K, Peterson WM, Cairns DS. Selective activation of intrinsic cohesive elements. J Appl Math Phys 2014;2:1061–8. https://doi.org/10.4236/jamp.2014.212121.

[34] Hashin Z. Failure criteria for unidirectional fibre composites. J Appl Mech 1980;47(2):329–34. https://doi.org/10.1115/1.3153664.

[35] Chang FK, Chang KY. A progressive damage model for laminated composites containing stress concentrations. J Compos Mater 1987;21:834–55. https://doi.org/10.1177/002199838702100904.

[36] Alfano G, Crisfield MA. Finite element interface models for the delamination analysis of laminated composites: mechanical and computational issues. Int J Numer Methods Eng 2001;50(7):1701–36. https://doi.org/10.1002/nme.93.

[37] Geleta TN, Woo K, Lee B. Delamination behavior of L-shaped laminated composites. Int J Aeronaut Space Sci 2018. https://doi.org/10.1007/s42405-018-0038-y.

[38] Benzeggagh ML, Kenane M. Measurement of mixed-mode delamination fracture toughness of unidirectional glass/epoxy composites with mixed-mode apparatus. Compos Sci Technol 1996;56(4):439–49. https://doi.org/10.1016/0266-3538(96)00005-X.